# Determination of Gravity-Induced Deformations of Heliostat Structures through Flux Maps Analyses

**Alejandro Martínez Hernández[1], Iván Bravo Gonzalo[1], Manuel Romero[1] and José González Aguilar[1]**

[1] IMDEA Energy Institute, Avda. Ramón de la Sagra 3, 28935 Móstoles (Spain)

**Abstract**

Heliostat optical performance can be affected by gravity-induced deformations in the structure that supports the mirror. These deformations can result in optical and pointing errors that increase the spillage and, therefore, decrease the energy collection efficiency. In this work, a method for determining the deformation degree of a heliostat structure under gravity loads is presented. This method is based on the comparison between experimental and numerical flux maps at different times of the day. Numerical flux maps are simulated using matrices of slope errors determined through deflectometry. For each heliostat, its matrix of slope errors is determined for a specific orientation of its structure depending of the heliostat position in the field. If there is no gravity-induced deformation, the experimental flux map acquired at any time of the day should be identical to its corresponding numerical one. On the contrary, if deformation exists, there should be differences between both maps depending on the orientation of the heliostat, i.e., on the time of the day. Quantitative comparison between both maps is carried out statistically with the root mean square deviation and the Pearson correlation coefficient. For this study, the heliostat solar field located at IMDEA Energy in Mostoles, Spain, is used.

*Keywords: Ray-tracing, Deflectometry, Solar Field, Heliostat, Concentrated Solar Power, Flux Map*

## 1. Introduction

Heliostats are employed in solar thermal power plants to concentrate solar radiation and produce heat for electricity generation. In order to maximize the energy collection efficiency, the stiffness of the heliostat structure plays an important role. A low stiffness can result in mirror deformations due to gravity and wind loads (Strachan and Houser, 1993), what produces optical and pointing errors, thus reducing the optical efficiency and performance of the heliostat. In order to avoid these deformations, the stiffness of the heliostat structure should be as high as possible, but increasing the stiffness of the structure also increases the cost of the heliostat, so a trade-off between both must be reached.

Several studies have been carried out investigating the effect of static loads, such as gravity, on solar concentrators (Meiser et al., 2016). All these studies are based on FEA (Finite Element Analysis) models that predict the displacement of the concentrator structure under different static loads. For heliostats, inexpensive methods to validate these FEA models have been proposed (Moya and Ho, 2011), and the influence of the deformations provided by these FEA models on the flux maps has been investigated (Yuan et al., 2015).

In this work, a novel methodology that allows determining the existence or not of gravity-induced deformations in the structure of a heliostat is proposed. This methodology is based on the analysis of experimental and numerical flux maps and allows quantifying the influence of gravity-induced deformations on flux maps without using FEA models, so information about optical and pointing errors is directly obtained. However, even though FEA models are not needed, this method requires to previously characterize the surface of the heliostat. In the next sections, the methodology developed here is described in detail and applied to the heliostats of the solar field located at IMDEA Energy in Mostoles, Spain (Romero et al., 2017).

© 2019. The Authors. Published by International Solar Energy Society
Selection and/or peer review under responsibility of Scientific Committee
doi:10.18086/swc.2019.18.03 Available at http://proceedings.ises.org

## 2. Methodology and experimental set-up

### 2.1 Methodology

The method developed here consists of measuring experimental flux maps for different orientations of a heliostat, i.e., for different times of the day, and then comparing them with their respective numerical maps. In order to generate these numerical maps, matrices of the slope error of the mirror surface in x and y directions must be known. For this, deflectometry (Ulmer et al., 2010) or another surface characterization technique that provides this information must be used first. In this case, deflectometry has been performed to some heliostats of the solar field. Deflectometry is performed projecting a stripe pattern over a target located in the tower and analyzing the reflected image of this pattern over the surfaces of the heliostats by a camera also located in the tower. Thus, deflectometry is performed for a single orientation of the heliostat that depends on its position in the solar field, while experimental flux maps are acquired for different orientations of the heliostat depending on the time of the day. Therefore, if no gravity-induced deformation exists, both numerical and experimental flux maps should be equal at any time of the day. On the contrary, if deformation exists, only the experimental flux map acquired at the same heliostat position as for the deflectometry measurement should be equal to the numerical flux map.

Comparison of numerical and experimental flux maps is performed through the calculation of the root mean squared deviation, RMSD, and the Pearson correlation coefficient, $\rho$.

$$RMSD = \sqrt{\frac{1}{N}\sum_{i=1}^{N}\left(I_{exp,i} - I_{num,i}\right)^2} \quad \text{(eq. 1)}$$

$$\rho = \frac{\sigma_{exp,num}}{\sigma_{exp}\sigma_{num}} = \frac{\sum_{i=1}^{N}\left(I_{exp,i}-\overline{I_{exp}}\right)\left(I_{num,i}-\overline{I_{num}}\right)}{\sqrt{\sum_{i=1}^{N}\left(I_{exp,i}-\overline{I_{exp}}\right)^2}\sqrt{\sum_{i=1}^{N}\left(I_{num,i}-\overline{I_{num}}\right)^2}} \quad \text{(eq. 2)}$$

In equations (1) and (2) $\sigma_{exp,num}$ is the covariance between both experimental and numerical flux maps, $\sigma_{exp}$ and $\sigma_{num}$ are their standard deviations, $N$ is the number of elements of the matrices associated with the flux maps, $I$ is the irradiance of each element of the matrices and $\bar{I}$ is the average irradiance of the map. As we are only interested in the shape of the flux maps and as it does not depend on the value of the DNI (Direct Normal Irradiance), both numerical and experimental flux maps are normalized before comparing them. In this way, we can use any value of the DNI to simulate the flux map, so the pyrheliometer uncertainty is eliminated. Moreover, normalization of the experimental flux map also eliminates the radiometer uncertainty.

The main difficulty for calculating the Pearson correlation coefficient is that both experimental and numerical maps must be perfectly superposed. For doing this, an algorithm that determines the best superposition between the two maps has been developed. Assuming that r and c are the number of rows and columns, respectively, of the matrices associated with the flux maps, there are (2r-1)(2c-1) overlapping possibilities between both maps (see Fig. 1). This algorithm calculates the RMSD for each of those possibilities, with the superposition with the minimal value of the RMSD being the best overlapping possibility. Once the best overlapping possibility has been found, the Pearson correlation coefficient is calculated.

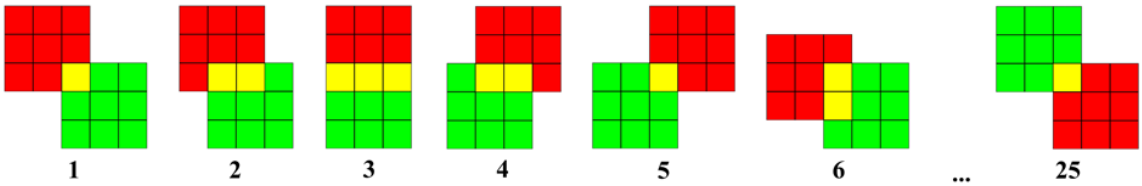


**Fig. 1: Overlapping possibilities between the flux maps. The green matrix is associated with the numerical flux map, and the red matrix is associated with the experimental flux map. For the first overlapping possibility, the first element of the green matrix is compared with the last element of the red matrix, and the rest of the elements of the green matrix are compared with zero, since there is no radiation outside of the target. This is only true if the target is large enough to intercept all the beam.**

To correctly compare different pairs of numerical and experimental flux maps with the Pearson correlation coefficient, the relative size of the target compared to that of the beam must be taken into account. For instance, if the size of the target is much bigger than the size of the beam, the Pearson correlation coefficient will tend to the unity even if the experimental and numerical maps are quite different. This is because the irradiance of the vast majority of the elements of both matrices will have the same value, zero. For this reason, the Pearson correlation coefficient must be calculated only for those values of irradiance higher than a certain limit. In this way, zero irradiance values are excluded. This cut-off of the irradiance level has been established at 1/15 of the maximum irradiance.

## 2.2 Numerical flux maps

Numerical flux maps have been obtained through ray-tracing simulations performed with a custom ray-tracing software developed with Matlab. This software has been validated comparing its simulations with simulations performed with a commercially available ray-tracing software, TracePro®. The reason for using this ray-tracing program instead of TracePro® or other commercial software is its capability to perform simulations with several millions of rays in a very small amount of computation time. This custom program works dividing the heliostat reflective surface into small elements and tracing rays from each one of these elements. For this study, simulations have been performed tracing a bundle of 2500 sunrays per reflecting element of the heliostat surface, with a total of 486400 square reflecting elements per heliostat (1.216 billion of rays) of 0.25 cm side each one. The normal vector of every reflecting element is known due to the deflectometry measurements. Each sunray of the bundle is deflected from the main direction of the reflected sun vector according to the given sunshape distribution. In this case, simulations have been performed employing the limb-darkened distribution (Romero et al., 2016). The 1.216 billion of rays are traced over a square target of 110 cm side divided in square elements of 1 cm side.

The accuracy of the superposing algorithm depends on the relation between the size of the beam and the size of the elements in which the target is divided. Therefore, in order to increase the accuracy of the superposing algorithm, the length of these elements should be as small as possible. But the smaller the length, the higher the number of rays needed in order to get a numerical flux map with an equitable distribution of them, which yields a higher computation time. For this reason, a compromise between the computation time and the accuracy of the overlapping algorithm must be found. In this case, in order to increase the accuracy without increasing the computation time when tracing more rays, the numerical flux maps were up-sampled by a factor of 2 using a spline interpolation, and thus numerical and experimental maps were centered with an uncertainty of 0.5 cm.

## 2.3 Experimental flux maps

Experimental flux maps were acquired using a flux mapping acquisition system (Thelen et al., 2017), which is based on a CCD camera (Prosilica GT1930L, Allied Vision Technologies) and a square Lambertian target of 110 cm side located at a height of 13 meters in vertical position. The resolution of the flux maps is about 1 mm per pixel, so the dimensions of the matrices associated with the experimental flux maps are higher than the dimensions of the matrices associated with the numerical flux maps. However, in order to apply the overlapping algorithm both matrices must have the same dimensions, so a down-sampling of the experimental flux maps was performed to match the numerical flux maps dimensions.

## 2.4 The heliostats

The heliostats of the solar field located at IMDEA Energy in Mostoles, Spain, have been used as a test case. This solar field is composed of 169 heliostats of 3 $m^2$ reflective surface distributed in 14 rows. Each heliostat consists of one small facet of 1.6 m x 1.9 m, 3 mm thickness and 94.3% of reflectivity. The facet is bonded with a black adhesive silicone paste to a curved support structure which gives the mirror the desired focal length. Two focal lengths have been employed in the field: 20 m for the first 8 rows of the field (84 heliostats), and 30 m for the last 6 rows (85 heliostats). For this work, 5 heliostats with short focal length and 4 heliostats with large focal length have been tested. Figure 2a shows the distribution of the heliostats in the field as well as the heliostats that has been tested (red ones). Figure 2b shows the heliostat structure and the tracking system. This is based on tilt and roll motions instead of the common tracking systems based on azimuth-elevation (Chong and Wong, 2009).

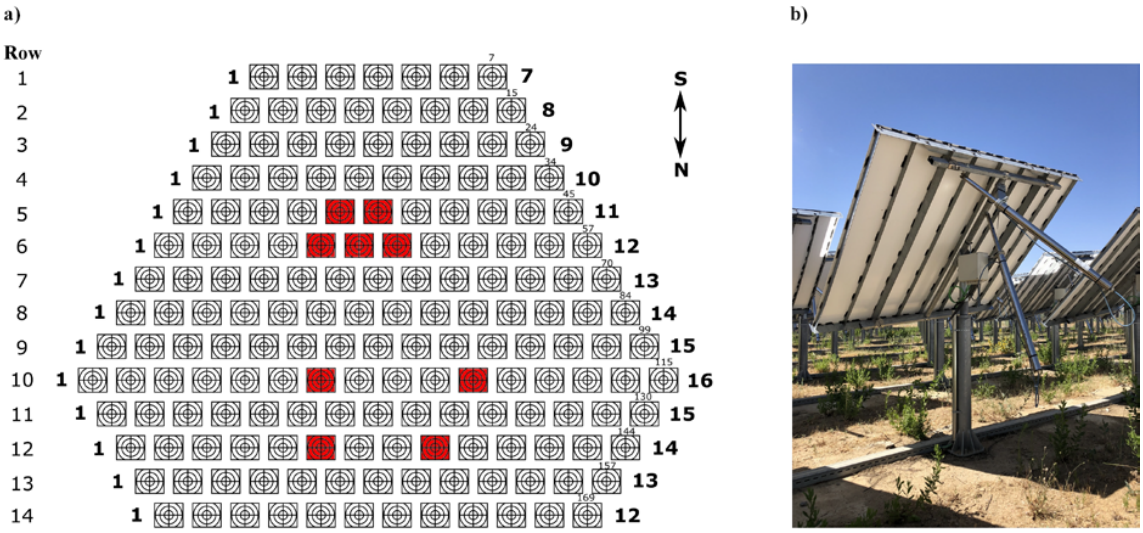


**Fig. 2: a) Distribution of the heliostats on the field. The tested heliostats are marked in red. b) Heliostat structure and tracking system**

Table 1 shows the optical characteristics of the 9 heliostats tested: nominal focal length, real focal length and slope error (last two determined through deflectometry measurements). Furthermore, heliostat-target distance is shown. The notation employed for denoting heliostats is m-n, where m refers to the row number, starting to count from the south, and n is the position of the heliostat in the row, starting to count from the east.

**Tab. 1: Optical characteristics of the heliostats and heliostat-target distances**

| Heliostat | Nominal focal length (m) | Real focal length (m) | Heliostat-target distance (m) | Slope error x (mrad) | Slope error y (mrad) |
|---|---|---|---|---|---|
| 5-5 | 20 | 22.3 | 17.3 | 2.04 | 2.24 |
| 5-6 | 20 | 22.0 | 17.1 | 1.39 | 1.62 |
| 6-5 | 20 | 22.7 | 19.2 | 1.35 | 1.51 |
| 6-6 | 20 | 21.5 | 18.8 | 2.16 | 2.58 |
| 6-7 | 20 | 22.4 | 18.8 | 1.35 | 1.36 |
| 10-7 | 30 | 32.3 | 26.8 | 0.83 | 1.1 |
| 10-11 | 30 | 31.2 | 27.3 | 0.72 | 0.86 |
| 12-6 | 30 | 34.6 | 30.9 | 1.10 | 1.01 |
| 12-9 | 30 | 30.6 | 30.9 | 0.96 | 1.09 |

## 3. Results

Several flux maps have been acquired for each heliostat from three hours before solar noon to three hours after. Flux maps were acquired on 15$^{th}$ January, 2019. For this day, solar noon was at 13:24 local time. Table 2 shows the local time when flux maps have been acquired. The red color indicates the time at which the heliostat position is closest to the deflectometry measurement position. Around solar noon, the shadow of the tower over some heliostats prevented from measuring their flux maps. Later, in the afternoon, the presence of some clouds did not allow to acquire as many flux maps as in the morning.

**Tab. 2: Local time when flux maps have been acquired for the nine heliostats tested. The red color indicates the time when the heliostat position is closest to the deflectometry measurement position.**

| Heliostat | 5-5 | 5-6 | 6-5 | 6-6 | 6-7 | 10-7 | 10-11 | 12-6 | 12-9 |
|---|---|---|---|---|---|---|---|---|---|
| Flux map acquisition time | 10:20 | 10:22 | 9:57 | 9:59 | 10:01 | 10:06 | 10:07 | 10:08 | 10:10 |
| | 10:43 | 10:45 | 10:23 | 10:25 | 10:28 | 10:33 | 10:34 | 10:36 | 10:38 |
| | 11:07 | 11:10 | 10:47 | 10:49 | 10:52 | 10:55 | 10:57 | 10:59 | 11:00 |
| | 11:27 | 11:30 | 11:11 | 11:14 | 11:15 | 11:18 | 11:19 | 11:21 | 11:22 |
| | 11:49 | 11:52 | 11:31 | 11:33 | 11:35 | 11:39 | 11:40 | 11:42 | 11:43 |
| | 12:10 | 12:11 | 11:53 | 11:55 | 11:57 | 12:02 | 12:00 | 12:03 | 12:04 |
| | 12:31 | 12:33 | 12:13 | 12:15 | 12:16 | 12:20 | 13:09 | 12:23 | 12:25 |
| | 12:56 | 14:24 | 12:35 | 12:37 | 13:58 | 12:43 | 13:33 | 12:46 | 13:37 |
| | 14:56 | 14:58 | 12:59 | 13:01 | 14:36 | 13:07 | 14:11 | 13:10 | 14:14 |
| | 16:15 | 16:16 | 13:25 | 14:35 | 15:03 | 13:32 | 14:43 | 14:44 | 14:45 |
| | 16:32 | 16:34 | 16:18 | 15:01 | 16:22 | 14:41 | 15:08 | 15:10 | 15:12 |
| | | | | 16:20 | | 15:07 | 16:27 | 16:28 | 16:29 |
| | | | | | | 16:25 | | | |

Figure 3 shows the experimental and numerical flux maps of the heliostat 5-5 at 10:20 local time. Only normalized irradiance values above the cut-off level are shown. The area of each map with such irradiance levels has been calculated and is shown in the upper part of the figure. Additionally, Fig. 4 shows the overlay of both flux maps before and after applying the overlapping algorithm.

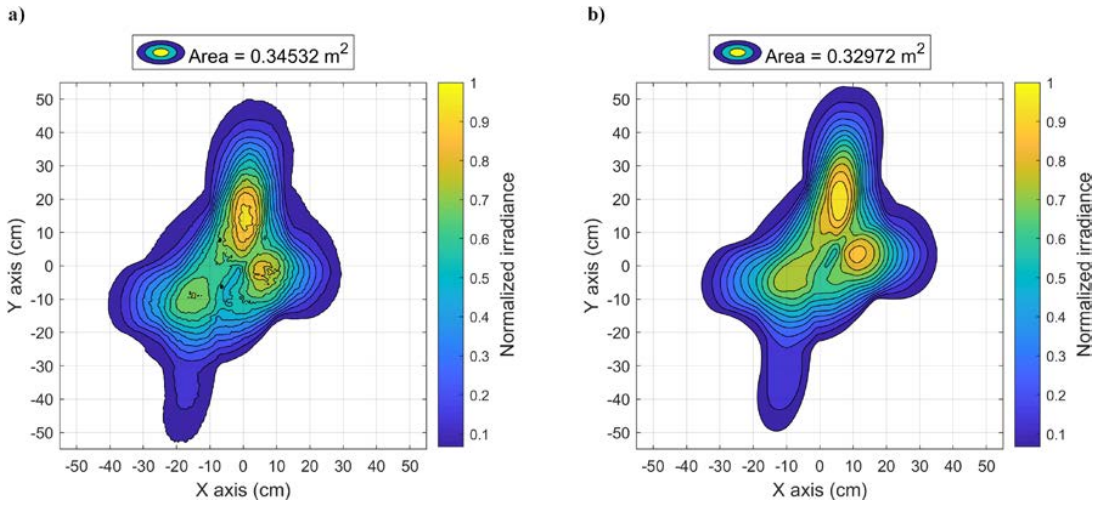


**Fig. 3: Flux maps of the heliostat 5-5 at 10:20 local time. a) Experimental flux map. b) Numerical flux map**

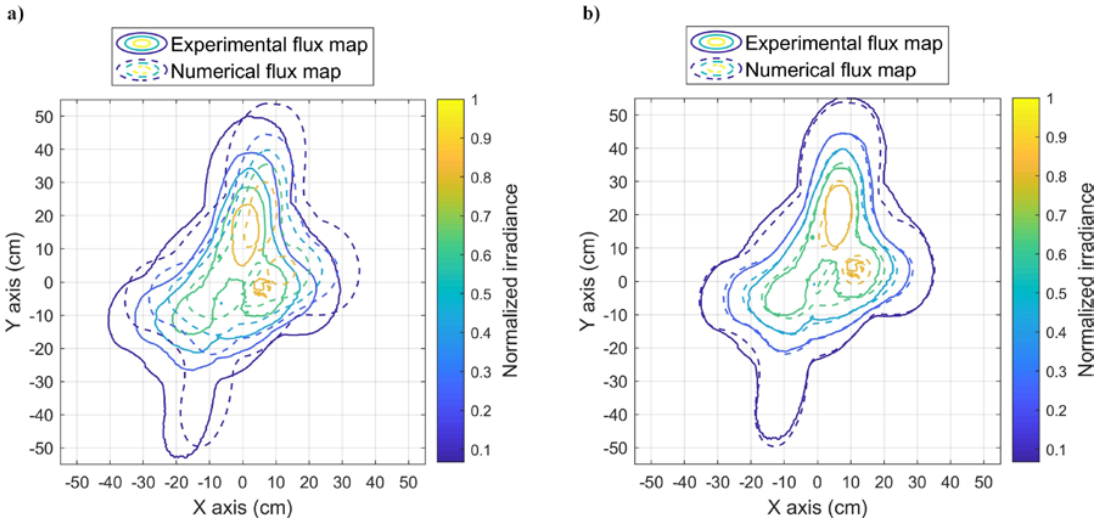


**Fig. 4: Overlay of the experimental and numerical flux maps of the heliostat 5-5 at 10:20 local time. a) Before applying the overlapping algorithm. b) After applying the overlapping algorithm**

It can be noted that the experimental map is slightly bigger than the numerical map. The same occurs for the rest of the flux maps acquired at other times of the day and for all the flux maps of the rest of the heliostats. The relative size differences have been calculated and are plotted in Fig. 6a. These differences could be due to several reasons, but we believe that this effect is mostly the result of the sunshape used in the simulations, which does not include circumsolar radiation. The inclusion of a sunshape with a certain degree of circumsolar radiation would produce reflected rays with higher angles than the angle subtended by the solar disk, and thus possibly extending the beam. Another possible cause could be the scattering of the reflected light as a result of the dust accumulated on the mirror and also maybe the specular error of the mirror.

Figure 5 shows the nine pairs of experimental and numerical flux maps perfectly overlapped corresponding to the measurements at the time indicated in red in Tab. 2. Figure 6b shows the evolution of the Pearson correlation coefficient along the day for the nine heliostats.

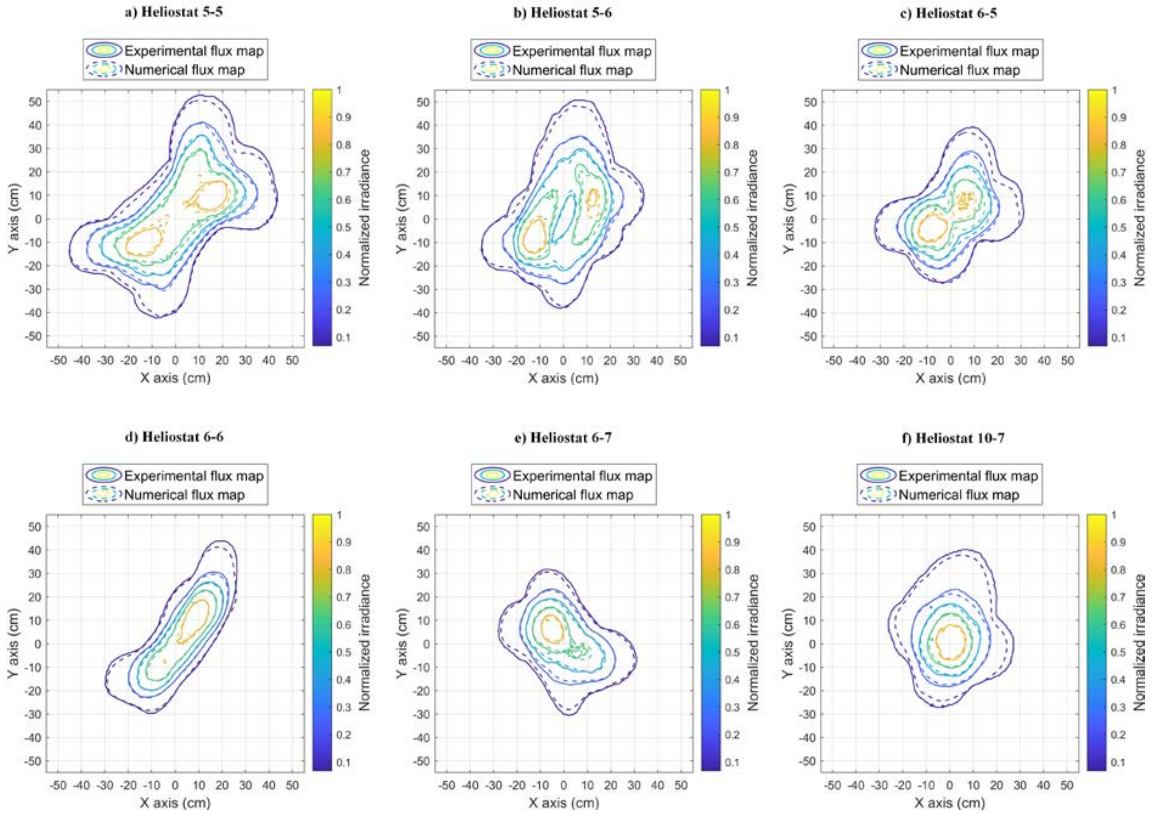

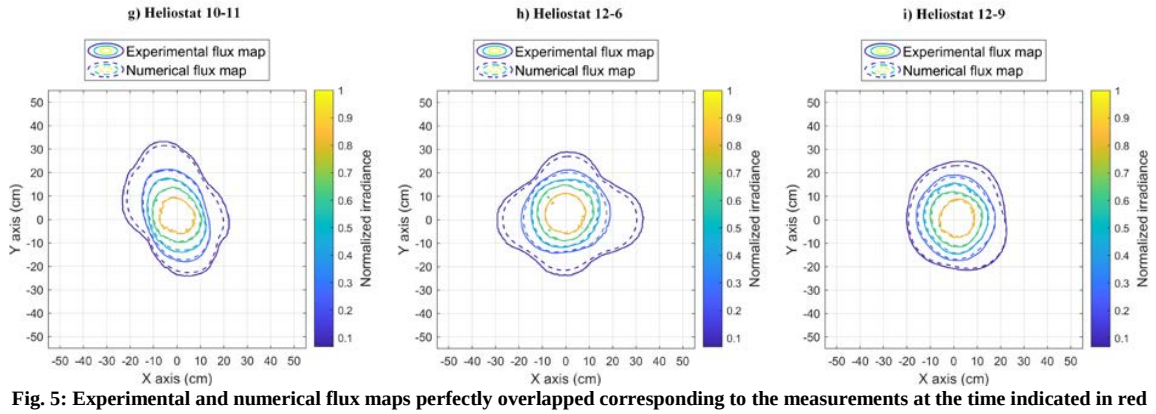


**Fig. 5: Experimental and numerical flux maps perfectly overlapped corresponding to the measurements at the time indicated in red in Tab. 2**

As explained before, it can be seen that the experimental flux maps are always slightly bigger than the numerical flux maps. Another interesting feature can be seen by comparing Fig. 4b and Fig. 5a, in which the flux maps of heliostat 5-5 at different times of the day (10:20 and 12:56, respectively) are shown. It can be noticed that the shape of the flux map changes dramatically. This behavior was expected and is due to the different orientation of the heliostat in relation to the target at each measurement. This occurs for all the heliostats and is more remarkable in the heliostats with large slope errors and with high differences between their focal length and their distance to the target.

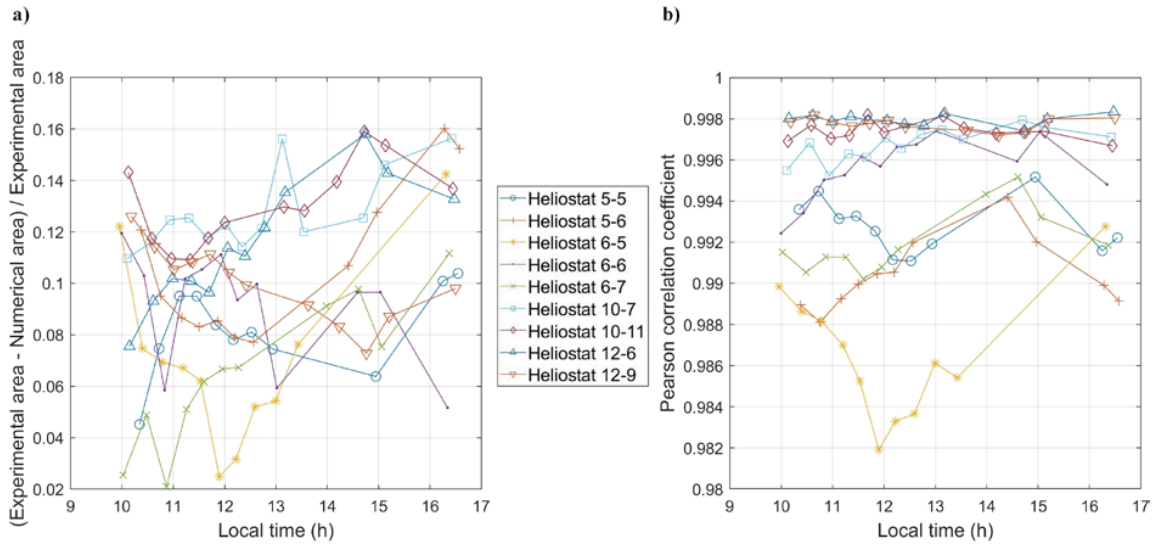


**Fig. 6: a) Relative size differences between experimental and numerical flux maps along the day for the nine heliostats. b) Pearson correlation coefficient along the day for the nine heliostats.**

Looking at Fig. 6b, it can be noticed that the Pearson correlation coefficient is higher for large focal length heliostats. This is due to their lower slope errors, what facilitates their characterization and simulation. For these heliostats, the Pearson correlation coefficient is constant along the day. For short focal length heliostats, the Pearson correlation coefficient suffers small variations, but there is no a common behavior among them. If deformations induced by gravity loads existed, the Pearson correlation coefficient would be maximum for the measurements at the time indicated in red in Tab. 2, and it would decrease before and after those. The absence of this behavior indicates that the structure of these heliostats is quite rigid and therefore it is not deforming while tracking the sun. Finally, it can be stated that the high correlation between numerical and experimental flux maps is remarkable, obtaining Pearson correlation coefficients higher than 0.98 in all cases, and thus proving the high accuracy of deflectometry measurements. These values of the Pearson correlation coefficient would be higher if the area differences between both flux maps were lower. To achieve this, as stated before, simulations should be performed employing a sunshape with a certain degree of circumsolar radiation.

## 4. Conclusions

A novel method for determining the deformation degree of the structure of a heliostat under gravity loads has been developed. This methodology has been applied to the heliostats of the solar field located at IMDEA Energy in Mostoles, Spain, which have shown high structural stability, not deforming at any position. This result is very important because it allows to dismiss mirror deformations as a source of optical and pointing errors, improving the optical efficiency and performance of the heliostat at the same time. It is well known that big heliostats composed of several facets suffer from deformation under gravitational loads, so the concept of small heliostat built from one single facet indeed represents an advantage due to its higher stiffness. As a future work, it would be very interesting to apply this method to bigger heliostats with known deformations.

The variety of shapes of the flux maps observed here shows the importance of optical characterization techniques, such as deflectometry, when simulating precise flux maps. In a similar way, fast ray-tracing tools are needed in order to perform studies like this in a reasonable time. While tracing only a few millions of rays is enough for common applications, such as prediction of the power over a receiver, several billions of rays are needed to obtain highly accurate flux maps. Otherwise, a high up-sampling factor of the numerical flux maps would be needed, which inherently introduces errors. Therefore, an effort should be done for developing new ray-tracing tools like the one developed and employed here.

## 5. Acknowledgments

The authors acknowledge support from the European Union for the project SUN-to-LIQUID Horizon 2020 Framework Programme (H2020) (654408). AMH acknowledge support from the Community of Madrid (Spain) through the Young Employment Program (PEJD-2017-PRE/AMB-4951).

## 6. References

Chong, K. K., & Wong, C. W., 2009. General formula for on-axis sun-tracking system and its application in improving tracking accuracy of solar collector. Solar Energy, 83(3), 298-305.

Meiser, S., Schneider, S., Lüpfert, E., Schiricke, B., & Pitz-Paal, R., 2017. Evaluation and assessment of gravity load on mirror shape and focusing quality of parabolic trough solar mirrors using finite-element analysis. Applied energy, 185, 1210-1216.

Moya, A. C., & Ho, C. K., 2011. Modeling and validation of heliostat deformation due to static loading. In ASME 2011 5th International Conference on Energy Sustainability (pp. 547-555). American Society of Mechanical Engineers.

Romero, M., González-Aguilar, J., Zarza, E., 2016. Concentrating solar thermal power, in: Goswami, D.Y., Kreith, F. (Eds.), Energy efficiency and renewable energy handbook, second ed. CRC Press, Boca Raton, Florida, USA, pp. 1237-1345.

Romero, M., González-Aguilar, J., & Luque, S., 2017. Ultra-modular 500 m2 heliostat field for high flux/high temperature solar-driven processes. In AIP Conference Proceedings (Vol. 1850, No. 1, p. 030044). AIP Publishing.

Strachan, J. W., & Houser, R. M., 1993. Testing and evaluation of large-area heliostats for solar thermal applications (No. SAND--92-1381). Sandia National Labs., Albuquerque, NM (United States).

Thelen, M., Raeder, C., Willsch, C., & Dibowski, G., 2017. A high-resolution optical measurement system for rapid acquisition of radiation flux density maps. In AIP Conference Proceedings (Vol. 1850, No. 1, p. 150005). AIP Publishing.

Ulmer, S., März, T., Prahl, C., Reinalter, W., &, Belhomme, B., 2010. Automated high resolution measurement of heliostat slope errors. Solar Energy 85 681–687

Yuan, J. K., Christian, J. M., & Ho, C. K., 2015. Compensation of gravity induced heliostat deflections for improved optical performance. Journal of Solar Energy Engineering, 137(2), 021016.